



Modulation of oxygen vacancy and zero-valent zinc in ZnCr_2O_4 nanofibers by enriching zinc for efficient nitrate reduction

Shuyue Dong^a, Aihui Niu^a, Kaihe Wang^a, Peiji Hu^a, Haoran Guo^{b,*}, Shengjun Sun^c,
Yongsong Luo^c, Qian Liu^d, Xuping Sun^{d,*}, Tingshuai Li^{a,*}

^a School of Materials and Energy, University of Electronic Science and Technology of China, Chengdu 611731, Sichuan, China

^b School of Chemical Sciences, University of Chinese Academy of Sciences, Beijing 100049, China

^c Institute of Fundamental and Frontier Sciences, University of Electronic Science and Technology of China, Chengdu 610054, Sichuan, China

^d Institute for Advanced Study, Chengdu University, Chengdu 610106, Sichuan, China

ARTICLE INFO

Keywords:

Nitrate reduction

Spinel

Oxygen vacancy

Theoretical calculation

ABSTRACT

One-step generation and modulation of oxygen vacancies by enriching zinc to substitute chromium ions in ZnCr_2O_4 nanofibers are proposed to reduce nitrate to ammonia, which meanwhile induces the formation of zero-valent zinc. The catalyst with the most oxygen vacancies achieves an optimal NH_3 yield rate of $20.36 \text{ mg h}^{-1} \text{ mg}_{\text{cat}}^{-1}$ and Faradaic efficiency of 90.21 % at -1.2 V vs. reversible hydrogen electrode (RHE), and it also has excellent long-term durability and structural stability. Theoretical calculations reveal oxygen vacancies are more favorable to form in ZnCr_2O_4 , which shift the d-band center (ϵ_d) of Cr and Zn to higher and lower energy levels, respectively. The free energy for the whole reaction on ZnCr_2O_4 shows a continuous decreasing tendency, indicating the reaction can spontaneously take place. The results are expected to pave a new avenue to rationally design defective non-noble catalysts for catalyzing nitrate to produce ammonia.

1. Introduction

Ammonia (NH_3) is a crucial raw material for chemicals, fertilizers, pharmaceuticals and plastic products [1], and is also regarded as a carbon-neutral energy carrier with high hydrogen storage ability and capacity density [2]. As a possibly environmentally-friendly alternative option to the century-old craft: Haber-Bosch process [3], electrocatalytic nitrogen reduction has attracted increasing recent attention for ambient ammonia production [4–6]. Although nitrogen gas is abundant in the atmosphere and easily available as the feeding gas, its performance is limited by the awfully strong triple bond and extremely low solubility in liquid systems [7,8]. Adhering to the concept of waste recycling and reuse, nitrate as the highest oxidation state of N offers us a more suitable source and its electroreduction has emerged as a promising approach to turn it into valuable NH_3 [9–12].

In essence, the electrochemical conversion of nitrate to NH_3 is a hydrogenation reaction, which competes with the hydrogen evolution reaction (HER) in the electrolyte. Besides, N-bearing species with various oxidation states may appear in the eight-electron transfer process [13], which abates the NH_3 -forming efficiency. Such issues can be

solved by utilizing electrocatalysts with excellent selectivity for NO_3^- reduction reaction (NITRR). Although noble metal catalysts perform efficiently for NITRR [14–17], the high price and scarcity vastly impede their widespread applications. Thus, considerable recent attention has been paid to designing and developing earth-abundant alternatives [10, 11, 18–23].

Spinel-type oxides with advantages of versatility, multivalence structure, flexible ion arrangement and high electronic conductivity have found electrochemical applications in batteries, supercapacitors and electrocatalysis [24–26]. Zinc (Zn) following iron (Fe) as the second most abundant transition metal in the human body, plays crucially biological roles in cell proliferation, immunologic function and resistance against free radicals [27–29]. In our early study, non electroactive Zn has been proven as an efficacious promoter to coordinate the HER performance of the CoP catalyst [30]. More recently, we have found that ZnO can enhance the NITRR performance of the Co_3O_4 catalyst [31]. It is well known that oxygen vacancies (Vos) can not only improve electrical conductivity by introducing defective energy levels in the forbidden band, which benefits charge transfer [32–37]. However, to the best of our knowledge, using ZnO for one-step Vo generation and modulation in

* Corresponding authors.

E-mail addresses: GuoHRan@163.com (H. Guo), xpsun@uestc.edu.cn (X. Sun), litingshuai@uestc.edu.cn (T. Li).

<https://doi.org/10.1016/j.apcatb.2023.122772>

Received 9 January 2023; Received in revised form 10 March 2023; Accepted 13 April 2023

Available online 14 April 2023

0926-3373/© 2023 Elsevier B.V. All rights reserved.

spinel oxides synergistic with zero-valent zinc (Zn^0) toward high-efficiency NO_3^- reduction electrocatalysis has not been reported so far.

In this work, the zinc-rich spinel ZnCr_2O_4 (ZCO) nanofiber is proposed as a high-performance NITRR electrocatalyst for ambient NH_3 synthesis, and the substitution of trivalent chromium with bivalent Zn ions effectively modulates the Vos, and boosts the electrocatalytic performance. In 0.1 M (the concentration of phosphate ions, both dissociated and undissociated) neutral phosphate-buffered electrolyte (PBS) with 0.1 M NO_3^- , such catalyst achieves a grate NH_3 yield of 20.36 $\text{mg h}^{-1} \text{mg}_{\text{cat}}^{-1}$ and a high Faradaic efficiency of 90.21% at -1.2 V vs. reversible hydrogen electrode (RHE). It also reveals excellent long-term durability and structural stability. Theoretical calculations demonstrate that the defective ZnCr_2O_4 has a large nitrate adsorption energy of -1.25 eV, and a minute ammonia desorption energy of 0.36 eV, while the maximum energy change is only 0.49 eV. The surplus Zn and Vos introduce more antibonding states, which lower the Fermi energy and thus synergistically enhance the performance.

2. Materials and methods

2.1. Preparation of materials

One-dimensional catalysts with different Zn: Cr ratios were prepared by electrospinning. 10 mL of a mixed solution of ethanol and DMF (1:1) was added to four beakers containing 1.6 g of $\text{Cr}(\text{NO}_3)_3 \cdot 9 \text{H}_2\text{O}$ and 0.60 g, 1.19 g, 1.79 g, 2.78 g of $\text{Zn}(\text{NO}_3)_2 \cdot 6 \text{H}_2\text{O}$, and the solutions were stirred until completely dissolved as liquid A. 1.6 g of PVP and 10 mL of mixed ethanol and DMF were stirred for 2 h until completely dissolved, and it was used as liquid B. At room temperature, solution A and solution B were mechanically mixed and magnetically stirred for 12 h as precursors for the four samples.

To conduct electrospinning, the syringe needle and the aluminum foil collector of the roller were kept at a distance of 15 cm, a negative voltage of -1.5 V and a positive voltage of 16.5 V were applied, and a feeding rate of 0.8 mL h^{-1} at 45°C was used with humidity below 35 %. The collected composite fibers were vacuum-dried at 60°C for 2 h to remove most of the organic reagents and then heated. For the first 1 h, the heating rate is 1°C min^{-1} to 200°C , then raised to 500°C within 2 h in a muffle furnace, which was naturally cooled and the products were successfully gained. ZnO nanofibers were prepared by the analogous method only with $\text{Zn}(\text{NO}_3)_2 \cdot 6 \text{H}_2\text{O}$, Zn comes from the reduction of ZnO, besides 2ZnO@ZCO is a simple mixture of ZnO and ZCO in a ratio of 2:1.

2.2. Characterization of materials

Scanning electron microscopy (SEM, Zeiss, Gemini 300) was used to characterize and analyze the one-dimensional microstructure and morphology. Phase identification was performed using high-resolution transmission electron microscopy (HR-TEM, FEI Tecnai F20) at 300 kV, equipped with energy dispersive spectroscopy (EDS, Zeiss Gemini 300) for elemental distribution mapping. A LabX XRD-6100 X-ray diffractometer with Cu K radiation at 0.154 nm called X-ray diffraction (XRD) was used to study the material composition. Under a high-purity nitrogen atmosphere, X-ray photoelectron spectroscopy (XPS) measurements were executed on an X-ray Photoelectron spectrometer (Thermal Fisher, USA, mono Al Ka (1486 eV)). Oxygen vacancy was detected by an electron spin resonance spectrometer in a dark environment (ESR, JES-FA200, JEOL, Japan). BET (fully automatic specific surface and porosity analysis) was detected using Quantachrome® ASiQwin™ at a testing temperature of 77.35 K with nitrogen as adsorbent. X-ray absorption fine structure data was collected by 1W1B station Synchrotron Radiation Facility (BSRF), which was recorded in a fluorescence mode.

2.3. Electrochemical measurements

The performance of electrochemical nitrate reduction on Zn-rich ZCO catalysts was tested with an H-type electrolytic cell. Using a Nafion membrane to separate the two-compartment cell. An electrochemical workstation (CHI660) carried out the electrochemical measurements. Confirming reference electrode with an Ag/AgCl/KCl electrode, and the counter electrode is a platinum foil electrode. Using Nafion as the protective film to make the working electrode, catalysts were deposited on the treated 1 cm^2 carbon paper. Typically, 655 μL ethanol and 325 μL deionized water were adopted to dissolve 5 mg catalyst with 20 μL of 5 wt% Nafion solution, which was then dispersed ultrasonically for 60 min to form homogeneous ink. Then, 20 μL of ink was coated on carbon paper ($\text{CP}, 1 \times 1 \text{ cm}^2$), which was dried at room temperature. For electrolyte, 0.1 M PBS solution with an extra 0.1 M NO_3^- reactant was adopted. all potentials mentioned below were adjusted to a reversible hydrogen electrode (RHE) as expressed by Eq. (1):

$$E(\text{vs.RHE}) = E(\text{vs.Ag/AgCl}) + (0.059 * \text{PH} + 0.197) \text{V} \quad (1)$$

2.4. Measurement of the ammonia yield

Nessler's reagent was used as the color reagent and the ultraviolet-visible (UV-Vis) was used for the determination of ammonia. In detail, the collected electrolytes were diluted 20 times, which exceeded the detection range because of the high concentration of NH_4^+ . Then, 2 mL of coloring agent (1 M NaOH solution including 5 wt% salicylic acid and the same proportion of sodium citrate), 1 mL of the oxidizing reagent (0.05 M sodium hypochlorite solution), and 0.2 mL catalyst solution (1 wt% dehydrated sodium nitroferrocyanide (III)) were slowly added in sequence to 2 mL diluted electrolyte. After sitting for 2 h in a lightless environment, UV-Vis absorption spectra were collected at 665 nm. A series of graded standard ammonium chloride solutions (65°C , 24 h) were prepared with dried ammonium chloride to calibrate the concentration-absorbance curve, which were used to calculate the ammonia yield in electrolyte after catalytic reaction.

2.5. Computational methods

Based on the HRTEM image and XRD pattern, First-principles calculations were performed using the Vienna Ab initio Simulation Package (VASP) to reveal the mechanisms of nitrate reduction reaction at the catalyst surfaces. More details are given in the [supplementary material](#).

3. Results and discussion

3.1. Characterizations of as-prepared catalysts

Fig. 1a illustrates the fabrication of the nanofiber (more details can be found in the experimental Section). Fig. 1b shows XRD patterns for four different ZCO catalysts with varying Zn contents, namely ZCO (ZnCr_2O_4), Z-ZCO ($\text{ZnO-ZnCr}_2\text{O}_4$), 2Z-ZCO ($2\text{ZnO-ZnCr}_2\text{O}_4$) and $^{11}\text{Z-ZCO}$ ($11\text{ZnO-3ZnCr}_2\text{O}_4$), respectively. Energy-dispersive X-ray spectroscopy (EDX) confirms the specific content for each element in the four specimens (Fig. S1 and Table S1) where the deviation of the real ratio indicates ZCO crystallinity is closely related to Zn content. The characteristic diffraction peaks match well with the standard ZCO and ZnO, indicating the co-existing of crystalline ZnO and ZnCr_2O_4 in nanofibers [38].

With the Zn ratio increasing, some peaks assigned to ZnO (JCPDS No. 79-2205) become more remarkable. Fig. 1c demonstrates that the concentration of Vo firstly increases with the content of Zn as detected by the electron spin resonance (ESR). When the ratio of Zn: Cr is 3:2, Vo reaches the high largest concentration and then it sharply decreases with the ratio increasing to 7:3. Random substitution of Zn^{2+} with Cr^{3+}

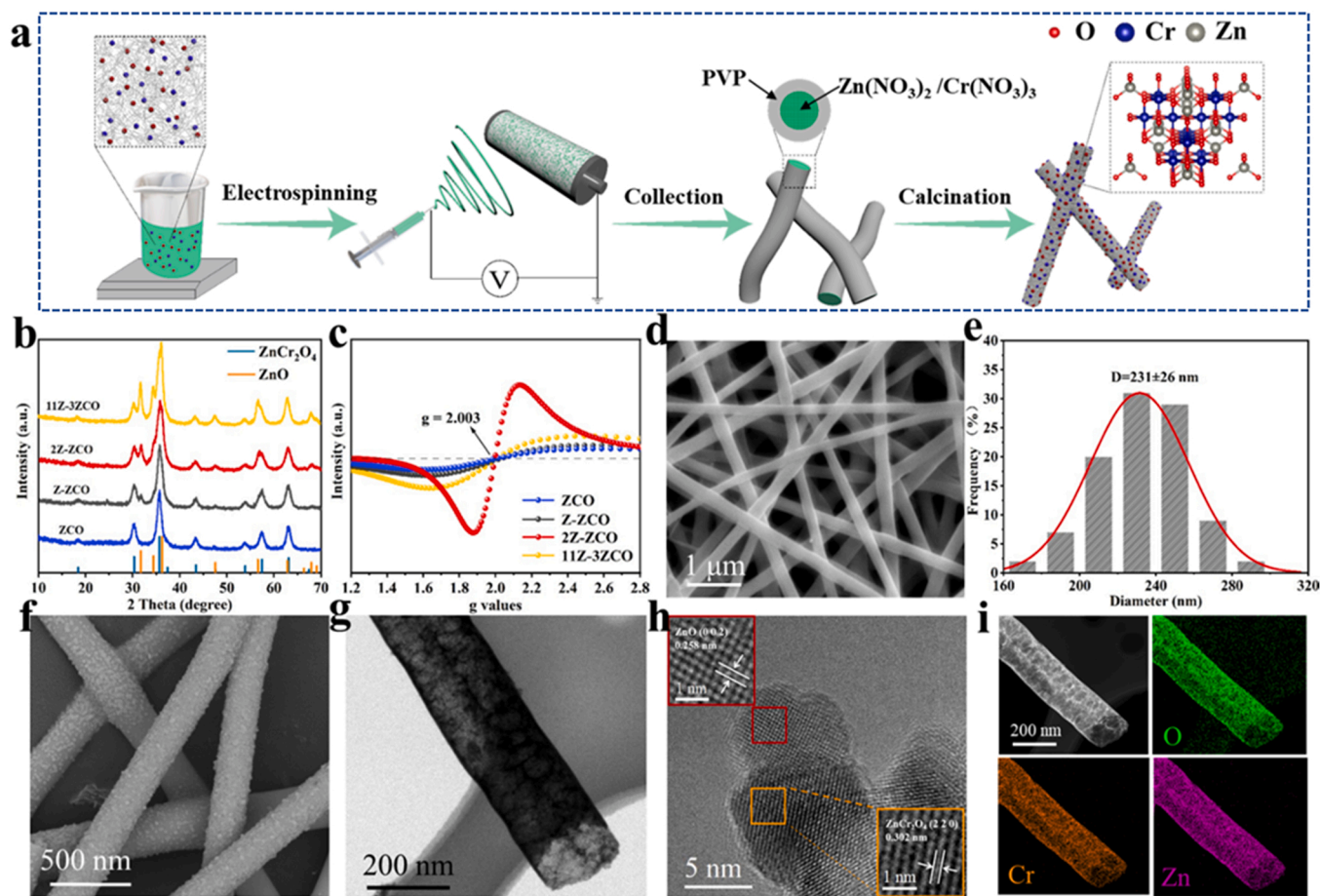


Fig. 1. (a) The sketch for the preparation procedures of Zn-rich ZCO. (b) X-ray diffraction patterns and (c) ESR spectra of ZCO, Z-ZCO, 2Z-ZCO and ¹¹Z-³ZCO. (d-f) SEM images of ZCO and diameter distribution of 2Z-ZCO. (g) TEM and (h) HRTEM image of 2Z-ZCO. (i) TEM image and corresponding EDX elemental mapping images of 2Z-ZCO.

octahedral sites leads to the formation of Vo, by which the dissolution of three ZnO species in ZnCr₂O₄ will create one Vo [39]. However, Vo is decreased with the increasing ratio of Zn: Cr to 7:3 possibly because more zinc ions and the increase of O_o^x in return occupy oxygen vacant positions [40]. Fig. 1d-f exhibit the scanning electron microscopy (SEM) image of 2Z-ZCO, where uniform fibers have an average diameter of around 231 nm and the fiber surface is coarse. The reasonably applied voltage is a key factor that guarantees the quality of fibers, so the distribution of the electric field is simulated (Fig. S2). The isotherms of N₂ adsorption/desorption of ZCO, Z-ZCO, 2Z-ZCO and ¹¹Z-³ZCO detected at conditions e are shown in Fig. S3a. BET measurements verify that ZCO has a very large specific surface area of 102.8 m² g⁻¹, significantly exceeding 63.74 m² g⁻¹ for Z-ZCO, 60.51 m² g⁻¹ for 2Z-ZCO and 46.25 m² g⁻¹ for ¹¹Z-³ZCO. The excessive Zn exsolved as zinc oxide particles at the ZCO surface will thus reduce Vos and surface area. Moreover, four catalysts have similar distributions of pore size with average pore widths of around 6.41 nm, 7.38 nm, 7.76 nm and 7.91 nm (Fig. S3b).

Transmission electron microscopy (TEM) image further confirms the straight fiber of 2Z-ZCO (Fig. 1g). Moreover, the high-resolution TEM (HRTEM) image shows the visible lattice spacing of 0.302 nm in ZCO (220) planes and 0.258 nm in ZnO (002) planes (Fig. 1h), in accordance with the XRD results. Noticeably, Zn, Cr and O are evenly dispersed in fibers according to EDX elemental mapping images (Fig. 1i). The single spinel ZCO also shows the same lattice and morphology (Fig. S4), indicating surplus Zn seldomly changes the catalyst microstructure. The morphology of Z-ZCO and ¹¹Z-³ZCO are shown in Fig. S5 and Fig. S6. The ZnO fibers are thoroughly characterized and confirmed by XRD,

SEM, TEM and ESR tests (Fig. S7-S8).

X-ray photoelectron spectroscopy (XPS) is used to reveal the valent states of each element in the four samples. The XPS survey spectra indicate the presence of Zn, Cr and O elements (Fig. S9) [41]. Fig. 2a shows nearly the same valent distributions of Cr, which well agrees with the previous report [42]. The simulative results present three components of Cr⁶⁺, Cr³⁺, Cr(OH)₃ or Cr₂O₃ on the surface [43]. The high-resolution Zn 2p spectra in Fig. 2b comprise the Zn 2p_{3/2} spin-orbit at 1021.4 eV and Zn 2p_{1/2} orbit at 1044.5 eV. The splitting energy of 21 eV between the two spin-orbits is equal to that of ZnO [44,45].

In Fig. 2c, the peaks at 529.6 eV and 531.0 eV correspond to the lattice oxygen (Zn-O bond or Cr-O bond) and Vo, respectively [46]. Ratios between the two oxygen states change regularly with the content of Zn, which perfectly supports the conclusion drawn from ESR results. All the aforementioned results definitely confirm the successful synthesis of the defective spinel ZCO nanofibers [47]. Fig. 2d shows the auger electron spectra of Zn LMM, where the relative content of zero-valent Zn is found to synchronously change with oxygen vacancy as shown in Fig. 2c [48,49]. X-ray absorption near-edge structure (XANES) and extended X-ray absorption fine structure (EXAFS) in depth reveal the local environment and structure around the Zn sites in 2Z-ZCO (Fig. S10 and Table S2). The existence of zero-valent Zn in 2Z-ZCO can be proved in Fig. 2e, where the intensity of 2Z-ZCO line peak is higher than the Zn foil but lower than ZnO. In Fig. 2f, the Zn-O shell peak can be observed at about 1.6 Å and 2.8 Å, while the Zn-Zn shell at 2.7 Å is discovered, validating the zero-valent Zn site configuration. The results are highly consistent with X-ray photoelectron spectroscopy (XPS) analysis. Fig. S11 shows the wavelet transform (WT) contour plots,

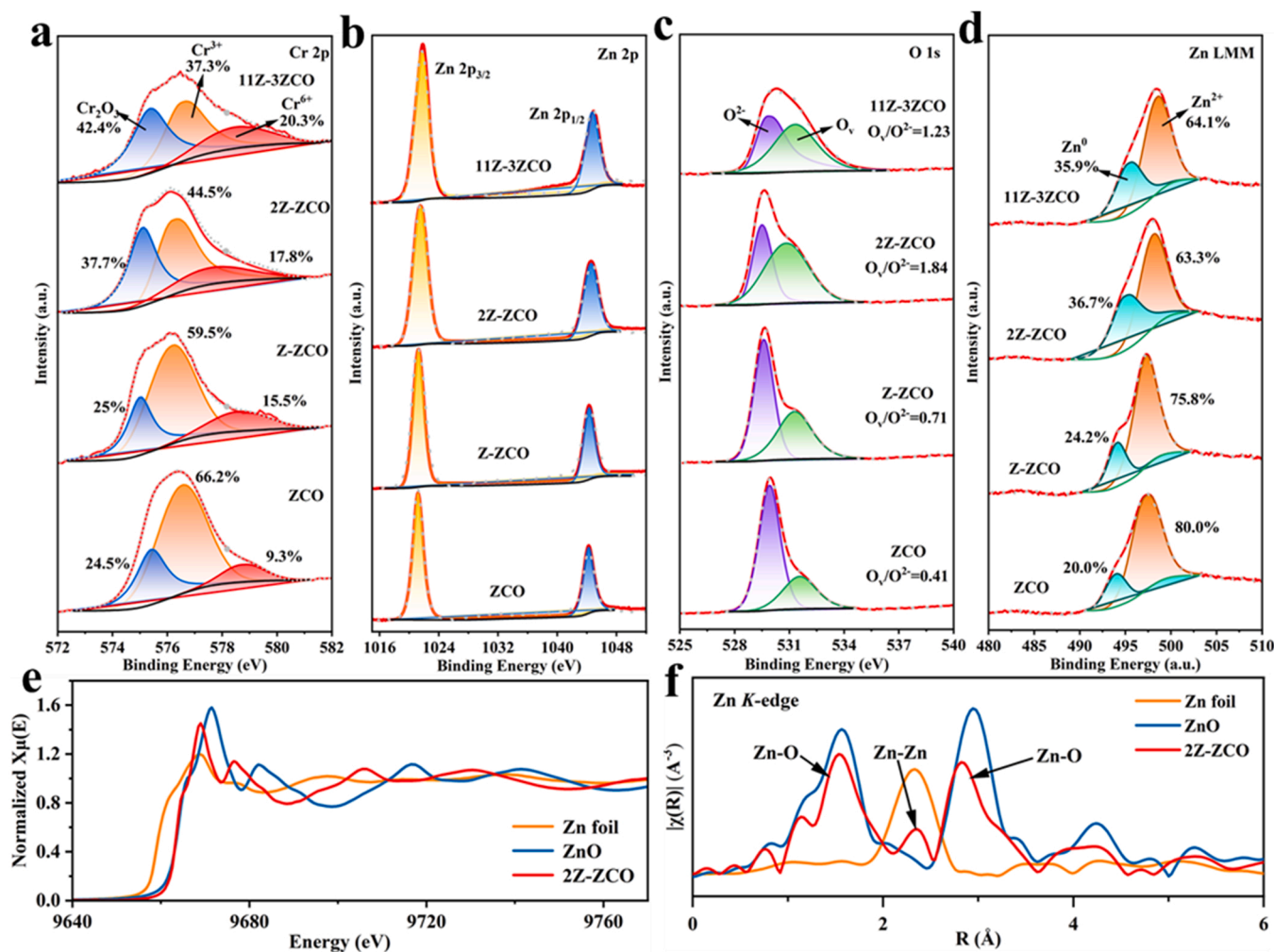


Fig. 2. XPS spectra of 2Z-ZCO in the (a) Cr 2p, (b) Zn 2p, (c) O 1s region and (d) Zn LMM. (e) Normalized XANES spectra at Zn K-edge. (f) Fourier-transformed EXAFS spectra correspondingly.

where the two main peaks are ascribed to the Zn-O and Zn-Zn contribution.

3.2. Measurements of electrochemical performance

In electrolytes with NO_3^- , LSV curves display a distinct increase in current density (Fig. 3a), suggesting the electroreduction of nitrate takes place. Nyquist plots of electrochemical impedance spectra (EIS) for the four spinel oxides indicate 2Z-ZCO has the smallest arc radius (Fig. 3b), implying this catalyst possesses low charge transfer resistance and large ion transport efficiency [50,51]. As shown in Fig. 3c, the Tafel slope of 2Z-ZCO (88 mV dec^{-1}) is smaller than the other three catalysts, corresponding to a faster kinetic reaction [52,53]. Calibration curves used for the determination of nitrate and nitrite concentrations are given in Fig. S12 and Fig. S13. Potentials ranging from -1.0 V to -1.4 V vs. RHE are applied on 2Z-ZCO to reduce nitrate (Fig. 3d and Fig. S14). The NH_3 yield increases.

steadily with the absolute voltage up to $30.32 (\pm 1.02) \text{ mg h}^{-1} \text{ mg}_{\text{cat}}^{-1}$, while the FE% presents a volcanic trend with a maximum value of $90.21 (\pm 1.80) \%$ at -1.2 V vs. RHE. There is a slight decline in more negative potentials due to competition with HER [54,55]. Therefore, the voltage at -1.2 V vs. RHE is selected as the optimal point to assess selectivity and durability. Moreover, 50.8 mg L^{-1} of NH_3 is detected by Ion Chromatography (IC), highly coincident with 51.7 mg L^{-1} measured by the ultraviolet and visible spectrum (UV-vis) method at the same electrolysis condition (Fig. S15). Compared with the pure ZnO, zinc

sheet or mechanically mixed powders (ZnO: ZCO=2:1) (Fig. 3e and Figs. S16), 2Z-ZCO with the most Vos reaches the best performance. The current density in Fig. S17 also shows the same changing tendency. 2Z-ZCO is superior to the other samples as given in Fig. S18-20, which further provides compelling pieces of evidence of the synergetic enhancing effects between ZnO and ZCO in the as-prepared nanofibers. Fig. S21 shows the effect of loading capacity of the catalyst on electrochemical performance. when the loading weight is 0.1 mg , the ammonia yield and Faraday efficiency are both greater than 0.05 mg and 0.2 mg , which is because too small catalytic dose is insufficient to cover the carbon paper of 1 cm^2 , so the partial carbon paper is naked to the solution and the efficiency is relatively low. However, too large catalytic dose may increase the catalyst thickness and enlarge resistance for electron transfer.

To deeply unveil the durability of 2Z-ZCO, the start-stop test (stop to collect and replace the electrolyte every 24 h for FE and NH_3 yield tests and restart the test at the same voltage) proceeded for 96 h (Fig. S22), and the current stays almost unchanged, which can avoid the effect of pH value on the performance [56]. Moreover, in 24 h electrolysis, negligible fluctuations in NH_3 yields and FEs are observed at varying point-in-time (Fig. 3f). The LSV curve and comparison of FE and NH_3 yield after the 24 h test also corroborate that the performance remains as usual (Fig. S23 and S24), which all indicate the catalyst is very stable.

To verify that the produced NH_4^+ solely originates from NITRR, the isotope labeling test is performed after electrolyzing $^{14}\text{NO}_3^-$ and $^{15}\text{NO}_3^-$ followed by product identification via ^1H NMR. Typical peaks of the ^1H

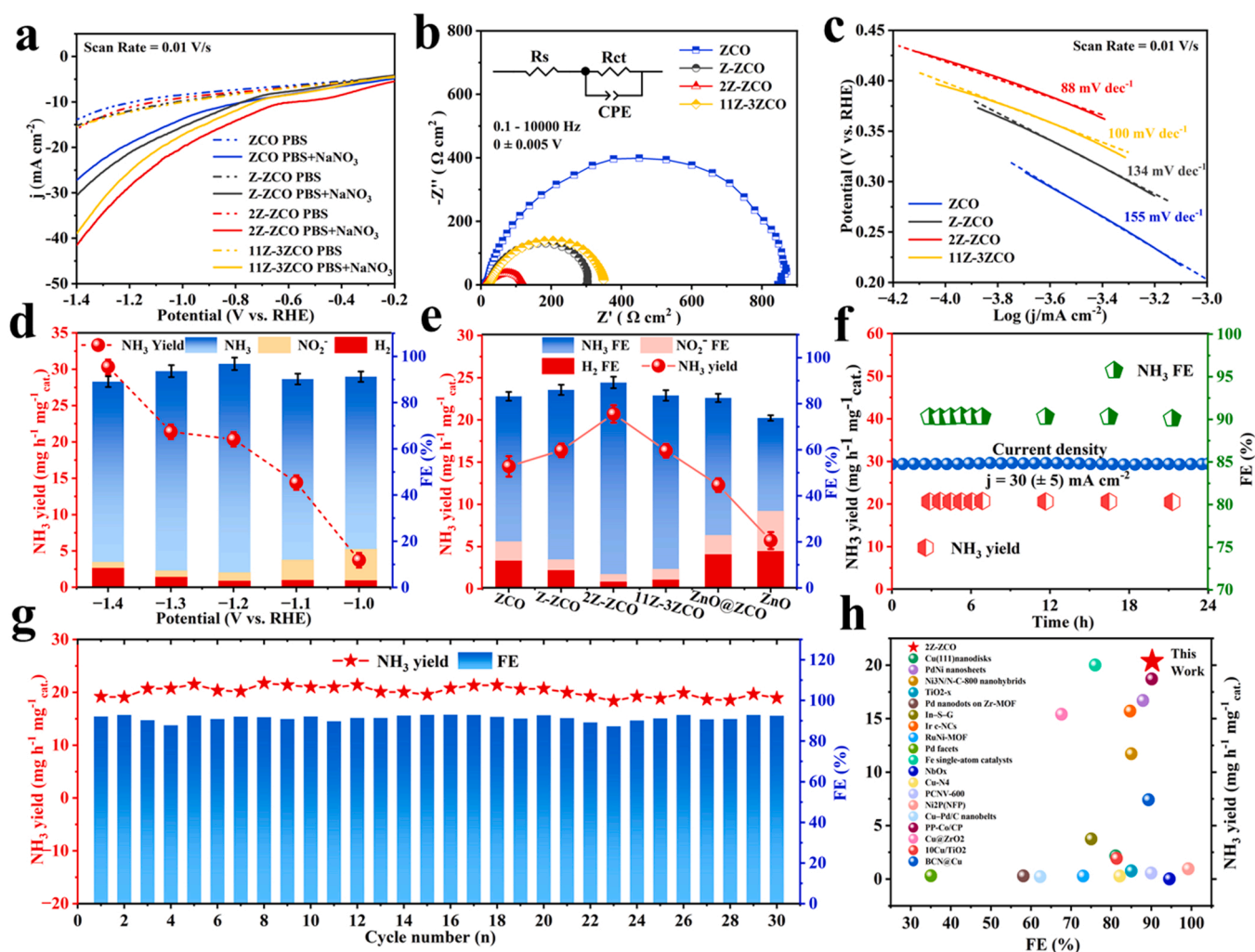


Fig. 3. (a) LSV curves in PBS with and without 0.1 M NaNO_3 . (b) EIS Nyquist plots of different catalysts. (c) Tafel plots of ZCO, Z-ZCO, 2Z-ZCO and $^{11}\text{Z}-^3\text{ZCO}$. (d) NH_3 yield and NH_3 FEs, NO_2^- FEs and H_2 FEs of 2Z-ZCO tested at varying applied potentials. (e) Electrocatalytic performance of various cathodes at the relevant optimal potentials (ZCO: -1.3 V vs. RHE, Z-ZCO: -1.2 V vs. RHE, 2Z-ZCO: -1.2 V vs. RHE, $^{11}\text{Z}-^3\text{ZCO}$: -1.2 V vs. RHE, $\text{ZnO}@^3\text{ZCO}$: -1.3 V vs. RHE, ZnO : -1.3 V vs. RHE) (f) Evolution of current, NH_3 yield, FEs of 2Z-ZCO with time at -1.2 V vs. RHE. (g) Consecutive 30-cycles at -1.2 V vs. RHE on 2Z-ZCO (the reaction period for each cycle is 1 h). (h) Comparison of NH_3 yield and FEs of 2Z-ZCO with the previously reported catalysts (See Table S3 in Supporting information for detailed references).

resonance consist of a triplet for $^{14}\text{NO}_3^-$ and each peak is split into obscure doublets for $^{15}\text{NO}_3^-$, which proves the occurrence of $^{14}\text{NO}_3^-$ and $^{15}\text{NO}_3^-$ reduction at the catalyst surface, respectively (Fig. S25) [11]. Subsequently, several control experiments were conducted to exclude the external disturbance (Fig. S26), and a negligible amount of NH_3 is detected. After 30 cycling tests at -1.2 V vs. RHE as exhibited in Fig. 3g and Fig. S27, NH_3 yield and Faradaic efficiency exhibit a slight fluctuation, which also confirms the splendid electrochemical durability. In brief, 2Z-ZCO for reducing nitrate into NH_3 in terms of NH_3 production and FEs is superior to most other relative catalysts as presented in Fig. 3h and Table S3. Chemical stability is another crucial factor for catalytic materials. Fig. S28 demonstrates the elementary composition of 2Z-ZCO as well as the microstructure subjected to the aging test remains intact. XPS spectra confirm that all the existing valences show tiny changes for the catalyst after the test (Fig. S29). According to the Inductively Coupled Plasma Optical Emission Spectrometer (ICP-OES) analysis, extremely low concentration of zinc ions in electrolyte after the catalytic reaction is detected as shown in Fig. S30, where its amount only accounts for 2.95 % of the mass of catalyst on carbon paper. Similarly, slight fluctuation of yield and FE can be found during the alternating electrolysis tests (Fig. S31).

Besides, a large electrochemically active surface area is beneficial to

improve electrocatalytic activity [57], which is thus evaluated by detecting the electrochemical double-layer capacitance (Fig. S32). The slope derived from linear fitting determines 2Z-ZCO to 1.06 mF cm^{-2} , much larger than 0.691 mF cm^{-2} for ZCO, 1.01 mF cm^{-2} for Z-ZCO and 0.889 mF cm^{-2} for $^{11}\text{Z}-^3\text{ZCO}$. After normalizing to the electrochemically active surface area according to $\text{CdI} = I/V$, $\text{ECSA} = \text{CdI}/(\text{Cs} \cdot A)$, where Cs of the specific capacitance of oxides is $60 \mu\text{F cm}^{-2}$ [58], NH_3 yield of 2Z-ZCO is thus equal to $1.17 \text{ mg h}^{-1} \text{ cm}^{-1}$, still superior to that of ZCO ($0.979 \text{ mg h}^{-1} \text{ cm}^{-1}$), Z-ZCO ($1.11 \text{ mg h}^{-1} \text{ cm}^{-1}$) and $^{11}\text{Z}-^3\text{ZCO}$ ($1.10 \text{ mg h}^{-1} \text{ cm}^{-1}$), suggesting the excellent NITRR performance of 2Z-ZCO substantially results from the intrinsic electrocatalytic activity.

Aqueous Zn- NO_3 battery is another effective way to estimate its ability to transform NO_3^- to NH_3 [23]. The battery with 2Z-ZCO as cathode hits a striking high-power density of 5.52 mW cm^{-2} at 8.42 mA cm^{-2} (Fig. S33), surpassing the Zn- NO_3 battery based on Pd/TiO_2 (0.87 mW cm^{-2}) [59] and some other reported metal- NO , metal- N_2 and metal- NO_3 batteries (Table S4). Furthermore, the output current density increases from 0 mA cm^{-2} with a more negative potential plateau up to 20 mA cm^{-2} at 0.1 V vs. Zn, which remains steady at varying current densities. Density functional theory calculations based on the first principle were conducted by constructing models for ZnO and ZCO with and without Vo to gain more insight into the reactive

mechanism of NITRR at catalyst surfaces (Fig. S34).

3.3. Material calculations

The pristine ZCO (220) has a nitrate adsorption free energy (ΔG (NO_3^-)) of -2.28 eV, indicating strong force occurs between the surface and the ions adsorbing nitrate (Fig. 4a). The charge density difference profile shows that electrons transfer from Cr and N to O atoms, while the N-O bond is weakened and the Cr-O is strengthened, respectively. The following reaction step ($^*\text{NO}_3 \rightarrow ^*\text{NH}_3$) shows a continuous decrease in free energy, which needs no more energy for the whole subsequent reaction. The energy-increasing step is the desorption of the NH_3 molecule ($^*\text{NH} \rightarrow \text{NH}_3(\text{g})$), which is a thermodynamic barrier with an energy uphill of 0.62 eV. When the Cr-O pair is replaced by Zn (ZnCr_2O_4 (Vo)), ΔG (NO_3^-) is increased to -1.25 eV due to the less orbital overlapping between O and Zn atoms according to the charge density difference.

Notably, the desorption-free energy of NH_3 is decreased to 0.36 eV, indicating that the NH_3 molecule can be more easily generated and desorbed, which ensures the continuity of the entire reaction. The ZnO (002) surface presents the potential determining step (PDS) at the

$^*\text{NO} \rightarrow ^*\text{N}$ step with an energy uphill of 0.72 eV (Fig. 4b). Upon the introduction of Vos, PDS is shifted from $^*\text{NO}_2$ to $^*\text{NO}$, and meanwhile the maximum energy change decreases to 0.49 eV. The interaction between Zn-O is weaker than the Cr-O bonds, which also facilitates the desorption of NH_3 .

As shown in Fig. 4c, the differential Electrochemical Mass Spectrometry (DEMS) test indicates that.

NH_3 is the main product in nitrate reduction reaction over 2Z-ZCO, where the relative signal intensity of NH_3 ($m/z = 17$) reaches 10^{-9} , more intense than the intermediate NO_2 ($m/z = 46$) of 10^{-12} , NO ($m/z = 30$) of 10^{-13} , NH_2OH ($m/z = 33$) of 10^{-13} and N_2 ($m/z = 28$) of 10^{-11} detected in four cycles of the LSV tests from -0.2 V to -1.4 V vs. RHE, which excludes the possible intermediates and is beneficial to gain more insight into the reactive pathways.

The energy for Vo formation ($E_{\text{form}}(\text{Vo})$) is calculated according to Eq. (2),

$$E_{\text{form}}(\text{Vo}) = E(\text{surface}) + 0.5E(\text{O}_2) - E(\text{surface} - \text{Vo}) \quad (2)$$

where $E(\text{surface})$, $E(\text{O}_2)$ and $E(\text{surface}-\text{Vo})$ represent the calculated energy of the pristine ZnO/ZCO surfaces, O_2 molecule and the surface with

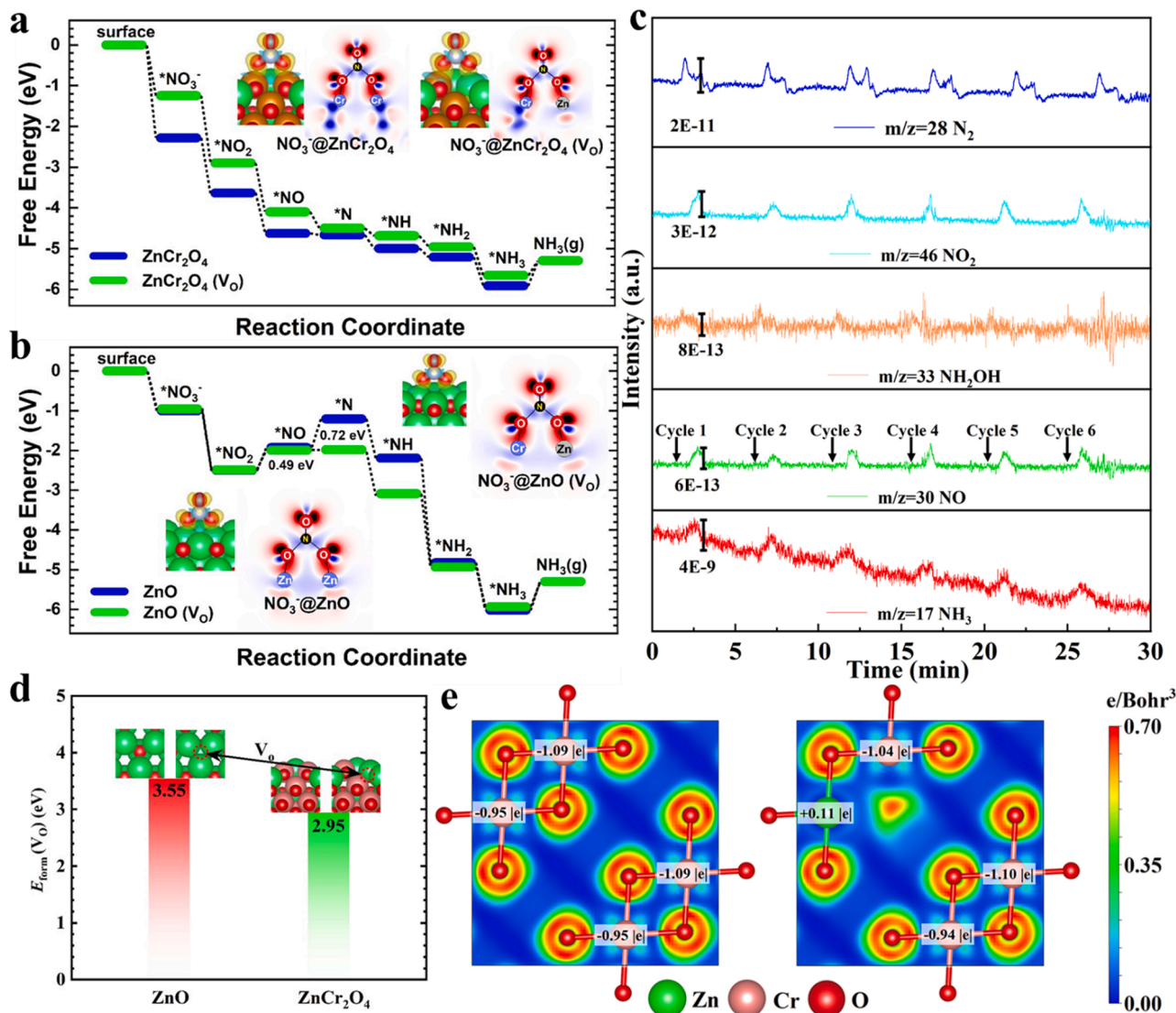
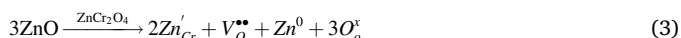


Fig. 4. Calculated free energy of (a) ZnCr_2O_4 and (b) ZnO with and without Vos. The charge density difference profiles of NO_3^- adsorbed on the two surfaces are illustrated in the Figures. Charge electron excess and electron-deficiency regions are marked in green and blue, respectively. (c) DEMS test of nitrate reduction to ammonia over 2Z-ZCO based on the LSV measurement by loading voltage ranges from -0.2 V to -1.4 V vs. RHE. (d) The energy for Vo formation $E_{\text{form}}(\text{Vo})$ at the ZnO and ZnCr_2O_4 surfaces. (e) The 2D electron localization function (ELF) slices of ZnCr_2O_4 and $\text{ZnCr}_2\text{O}_4\text{-Vo}$.

Vo models. As shown in Fig. 4d, the $E_{\text{form}}(\text{Vo})$ for ZCO presents a significant energy-decreasing trend compared with that for ZnO. Therefore, Vos are more favorable to form in ZnCr_2O_4 .

Furthermore, the valance changes of the atoms are evaluated by the Bader charge and electron localization function (ELF) calculations to theoretically reveal the Zn valance [60]. As shown in Fig. 4e, Cr atoms in the pristine ZCO unit cell present an external nuclear charge number ranging from $-0.95 \sim -1.09$ |e|, which is the same as Cr in the ZCO-Vo model. Due to the absence of the O atom induced by Zn^{2+} randomly replacing Cr^{3+} , the adjacent introduced Zn atom has a charge accumulation state with $+0.11$ |e| when the Cr-O combination is replaced by Zn and Vo. The charge bound by the O atom transfers to Zn, resulting in the formation of a zero-valence state of Zn as expressed by Eq. (3), which is well supported by the results in Fig. 2d and the XANES results in Fig. 2e and Fig. 2f,



where $2\text{Zn}'_{\text{Cr}}$ denotes the divalent zinc ion replacing the trivalent chromium ion with a negative charge, $\text{V}_{\text{O}}^{\bullet\bullet}$ the oxygen vacancy with two positive charges, O_o^x the lattice oxygen, Zn^0 the zero-valent zinc.

Furthermore, the migration processes of zero-valent Zn along two paths in ZCO-Vo are calculated (Fig. S35), which both exhibit large energy barriers of over 3 eV. Notably, the system energy of the potential cluster configuration (final state) is much higher than the initial dispersed state, indicating zero-valent zinc tends to be anchored nearby the oxygen vacancy instead of forming clusters or nanoparticles.

More orbital analyses indicate that Vo shifts the d-band center (ϵ_d) of Cr and Zn to higher and lower energy levels, which act as the main sites for nitrate adsorption and ammonia desorption, respectively (Fig. S36a). Based on the d-band center theory, the synergistic regulation of Cr and Zn modulates the free energy changes of the NITRR process by the stronger adsorption of NO_3^- and the weaker desorption of NH_3 molecules [61]. Furthermore, the Crystal Orbital Hamilton Populations (COHP) calculations between N-O and metal-O bonds indicate that insertions of Zn and Vo bring more antibonding states (Fig. S36b-c) [62]. Moreover, electrons can be transferred from the metal active sites to NO_3^- by the lone pair of electrons on the O atoms in combination with the half-occupied d-orbital of Cr. Therefore, NO_3^- can be reduced to NH_3 efficiently at the Zn-rich ZnCr_2O_4 surfaces.

The generation of Vo synchronously induces one zero-valent zinc and its content is coincident with the evolution of Vos as demonstrated by XPS results, so the catalytic activity is also discussed by calculating the free energy. As shown in Fig. S37, the PDS occurs at the $^*\text{NO}_2 \rightarrow ^*\text{NO}$ step with a free energy change of 0.24 eV, which presents enhanced catalytic performance compared to $\text{ZnO}(\text{Vo})$, but inferior to $\text{ZnCr}_2\text{O}_4(\text{Vo})$. The surplus zinc is beneficial to introduce oxygen vacancy and thus enhance catalytic performance. Besides, since the introduction of Vo plays a significant role in inhibiting hydrogen evolution and promoting electron transfer, the proton adsorption free energy (ΔG_{H}) at the ZnO , ZnO-Vo , ZCO and ZCO-Vo surfaces are calculated as shown in Fig. S38. ΔG_{H} for proton adsorption at ZnO , ZnO-Vo surfaces reach 2.34 eV and 2.73 eV, which makes it difficult both for hydrogen evolution and hydro-generation in nitrate reduction.

Notably, ΔG_{H} for ZCO is dramatically reduced to 0.47 eV, which increases to 1.28 eV with the formation of oxygen vacancy. Thus, the HER process is extremely weak to compete with NITRR over this catalyst. Especially, ΔG_{H} for zero-valent zinc reaches 0.55 eV, which indicates the generation of Zn^0 is also beneficial to suppress HER compared to ZCO. In addition, the conductivity of the catalyst is further evaluated by calculating the band structure. As shown in Fig. S39, the pristine ZCO shows a large band gap at the gamma point, in which the widths of the spin-up and spin-down electronic states are 2.68 and 3.88 eV, respectively, accounting for the low conductivity of ZCO. The Vo introduces vacant levels in the gap, reducing the gap widths to 1.58

and 1.40 eV for the spin-up and spin-down electrons, which thus improves the capability of electron transfer in the catalyst.

4. Conclusions

In summary, zinc is experimentally and theoretically verified as an effective promoter to generate and modulate Vos, which meanwhile induces zero-valent zinc synergistically boosting electrochemical nitrate reduction to NH_3 over ZnCr_2O_4 nanofibers. In 0.1 M PBS with 0.1 M NO_3^- electrolyte, such a catalyst is capable of achieving a large NH_3 yield rate of $20.36 \text{ mg h}^{-1} \text{ mg}^{-1}_{\text{cat}}$ and a high Faradaic efficiency of 90.21 % at -1.2 V vs. RHE with excellent long-term durability and chemical stability. This work not only offers an earth-abundant catalyst material for high-performance electrochemical nitrate-to- NH_3 conversion but would open up an exciting new avenue to the rational design of spinel oxides for electrocatalytic applications.

CRedit authorship contribution statement

Shuyue Dong : Methodology, Formal analysis, Investigation, Writing – original draft. **Aihui Niu**: Formal analysis. **Kaihe Wang**: Formal analysis. **Peiji Hu**: Formal analysis. **Haoran Guo**: Material calculation. **Shengjun Sun**: Investigation. **Yongsong Luo**: Investigation. **Qian Liu**: Investigation. **Xuping Sun**: Conceptualization, Validation, funding acquisition. **Tingshuai Li**: Methodology, Conceptualization, Resources, Supervision, Validation, Writing – review & editing.

Declaration of Competing Interest

The authors declare that they have no known competing financial interests or personal relationships that could have appeared to influence the work reported in this paper.

Data availability

No data was used for the research described in the article.

Acknowledgments

This work was supported by the National Natural Science Foundation of China (Nos. 22072015 and 21962013).

Appendix A. Supporting information

Supplementary data associated with this article can be found in the online version at doi:10.1016/j.apcatb.2023.122772.

References

- [1] X. Li, W. Fan, Y. Bai, Y. Liu, F. Wang, H. Bai, W. Shi, Photoelectrochemical reduction of nitrate to ammonia over CuPc/CeO₂ heterostructure: understanding the synergistic effect between oxygen vacancies and Ce sites, Chem. Eng. J. 433 (2022), 133225.
- [2] A. Klerke, C.H. Christensen, J.K. Nørskov, T. Vegge, Ammonia for hydrogen storage: challenges and opportunities, J. Mater. Chem. 18 (2008) 2304–2310.
- [3] S. Foster, S. Bakovic, R. Duda, S. Maheshwari, R. Milton, S. Minteer, M. Janik, J. Renner, L. Greenlee, Catalysts for nitrogen reduction to ammonia, Nat. Catal. 1 (2018) 490–500.
- [4] M. Shi, D. Bao, S. Li, B. Wulan, J. Yan, Q. Jiang, Anchoring PdCu amorphous nanocluster on graphene for electrochemical reduction of N₂ to NH₃ under ambient conditions in aqueous solution, Adv. Energy Mater. 8 (2018), 1800124.
- [5] Y. Yang, L. Zhang, Z. Hu, Y. Zheng, C. Tang, P. Chen, R. Wang, K. Qiu, J. Mao, T. Ling, S. Qiao, The crucial role of charge accumulation and spin polarization in activating carbon-based catalysts for electrocatalytic nitrogen reduction, Angew. Chem. Inter. Ed. 59 (2020) 4525–4531.
- [6] K. Chu, Y. Luo, P. Shen, X. Li, Q. Li, Y. Guo, Unveiling the synergy of O-vacancy and heterostructure over MoO_{3-x}/MXene for N₂ electroreduction to NH₃, Adv. Energy Mater. 12 (2022), 2103022.
- [7] Q. Liu, T. Xu, Y. Luo, Q. Kong, T. Li, S. Lu, A. Alshehri, K. Alzahrani, X. Sun, Recent advances in strategies for highly selective electrocatalytic N₂ reduction toward ambient NH₃, Synth., Curr. Opin. Electrochem. 29 (2021), 100766.

- [8] Y. Fang, Z. Liu, J. Han, Z. Jin, Y. Han, F. Wang, Y. Niu, Y. Wu, Y. Xu, High-performance electrocatalytic conversion of N_2 to NH_3 using oxygen-vacancy-rich TiO_2 in situ grown on $Ti_3C_2T_x$ MXene, *Adv. Energy Mater.* 9 (2019), 1803406.
- [9] Q. Liu, L. Xie, J. Liang, Y. Ren, Y. Wang, L. Zhang, L. Yue, T. Li, Y. Luo, N. Li, B. Tang, Y. Liu, S. Gao, A. Alshehri, I. Shakir, P. Agboola, Q. Kong, Q. Wang, D. Ma, X. Sun, Ambient ammonia synthesis via electrochemical reduction of nitrate enabled by $NiCo_2O_4$ nanowire array, *Small* 18 (2022), 2106961.
- [10] G. Chen, Y. Yuan, H. Jiang, S. Ren, L. Ding, L. Ma, T. Wu, J. Lu, H. Wang, Electrochemical reduction of nitrate to ammonia via direct eight-electron transfer using a copper-molecular solid catalyst, *Nat. Energy* 5 (2020) 605–613.
- [11] D. Liu, L. Qiao, Y. Chen, P. Zhou, J. Feng, C. Leong, K. Ng, S. Peng, S. Wang, W. Ip, H. Pan, Electrocatalytic reduction of nitrate to ammonia on low-cost manganese-incorporated Co_3O_4 nanotubes, *Appl. Catal. B Environ.* 324 (2023), 122293.
- [12] P. Langevelde, I. Katsounaros, M.T.M. Koper, Electrocatalytic nitrate reduction for sustainable ammonia production, *Joule* 5 (2021) 290–294.
- [13] H. Liu, J. Park, Y. Chen, Y. Qiu, Y. Cheng, K. Srivastava, S. Gu, B.H. Shanks, L. T. Roling, W. Li, Electrocatalytic nitrate reduction on oxide-derived silver with tunable selectivity to nitrite and ammonia, *ACS Catal.* 11 (2021) 8431–8442.
- [14] S. Guo, H. Li, K. Heck, X. Luan, W. Guo, G. Henkelman, M. Wong, Gold boosts nitrate reduction and deactivation resistance to indium-promoted palladium catalysts, *Appl. Catal. B Environ.* 305 (2022), 121048.
- [15] J. Li, G. Zhan, J. Yang, F. Quan, C. Mao, Y. Liu, B. Wang, F. Lei, L. Li, A. Chan, L. Xu, Y. Shi, Y. Du, W. Hao, P. Wong, J. Wang, S. Dou, L. Zhang, J. Yu, Efficient ammonia electrosynthesis from nitrate on strained ruthenium nanoclusters, *J. Am. Chem. Soc.* 142 (2020) 7036–7046.
- [16] H. Ren, S. Jia, J. Zou, S. Wu, X. Han, A facile preparation of Ag_2O/P_{25} photocatalyst for selective reduction of nitrate, *Appl. Catal. B Environ.* 176–177 (2015) 53–61.
- [17] G. Cerrón-Calle, A. Fajardo, C. Sánchez-Sánchez, S. García-Segura, Highly reactive Cu-Pt bimetallic 3D-electrocatalyst for selective nitrate reduction to ammonia, *Appl. Catal. B Environ.* 302 (2022), 120844.
- [18] Q. Chen, J. Liang, Q. Liu, K. Dong, L. Yue, P. Wei, Y. Luo, Q. Liu, N. Li, B. Tang, A. Alshehri, M. Hamdy, Z. Jiang, X. Sun, Co nanoparticle-decorated pomelo-peel-derived carbon enabled high-efficiency electrocatalytic nitrate reduction to ammonia, *Chem. Commun.* 58 (2022) 4259–4262.
- [19] Y. Zhao, Y. Liu, Z. Zhang, Z. Mo, C. Wang, S. Gao, Flower-like open-structured polycrystalline copper with synergistic multi-crystal plane for efficient electrocatalytic reduction of nitrate to ammonia, *Nano Energy* 97 (2022), 107124.
- [20] Z. Gong, W. Zhong, Z. He, Q. Liu, H. Chen, D. Zhou, N. Zhang, X. Kang, Y. Chen, Regulating surface oxygen species on copper (I) oxides via plasma treatment for effective reduction of nitrate to ammonia, *Appl. Catal. B Environ.* 305 (2022), 121021.
- [21] Z. Ge, T. Wang, Y. Ding, S. Yin, F. Li, P. Chen, Y. Chen, Interfacial engineering enhances the electroactivity of frame-like concave RhCu bimetallic nanocubes for nitrate reduction, *Adv. Energy Mater.* 12 (2022), 2103916.
- [22] Y. Yu, C. Wang, Y. Yu, Y. Wang, B. Zhang, Promoting selective electroreduction of nitrates to ammonia over electron-deficient Co modulated by rectifying Schottky contacts, *Sci. China Chem.* 63 (2020) 1469–1476.
- [23] R. Zhang, Y. Guo, S. Zhang, D. Chen, Y. Zhao, Z. Huang, L. Ma, P. Li, Q. Yang, G. Liang, C. Zhi, Efficient ammonia electrosynthesis and energy conversion through a Zn-nitrate battery by iron doping engineered nickel phosphide catalyst, *Adv. Energy Mater.* 12 (2022), 2103872.
- [24] C. Li, X. Han, F. Cheng, Y. Hu, C. Chen, J. Chen, Phase and composition controllable synthesis of cobalt manganese spinel nanoparticles towards efficient oxygen electrocatalysis, *Nat. Commun.* 6 (2015) 7345.
- [25] X. Zhao, L. Mao, Q. Cheng, J. Li, F. Liao, G. Yang, L. Xie, C. Zhao, L. Chen, Two-dimensional spinel structured co-based materials for high performance supercapacitors: a critical review, *Chem. Eng. J.* 387 (2020), 124081.
- [26] X. Liu, X. Cui, K. Dastafkan, H. Wang, C. Tang, C. Zhao, A. Chen, C. He, M. Han, Q. Zhang, Recent advances in spinel-type electrocatalysts for bifunctional oxygen reduction and oxygen evolution reactions, *J. Energy Chem.* 53 (2021) 290–302.
- [27] S.R. Powell, The antioxidant properties of zinc, *J. Nutr.* 130 (2000) 1447S–1454S.
- [28] T. Bray, W. Bettger, The physiological role of zinc as an antioxidant, *Free Radic. Biol. Med.* 8 (1990) 281–291.
- [29] N. Lim, H. Freake, C. Brückner, Illuminating zinc in biological systems, *Chem. Eur. J.* 11 (2005) 38–49.
- [30] T. Liu, D. Liu, F. Qu, D. Wang, L. Zhang, R. Ge, S. Hao, Y. Ma, G. Du, A. Asiri, L. Chen, X. Sun, Enhanced electrocatalysis for energy-efficient hydrogen production over CoP catalyst with nonelectroactive Zn as a promoter, *Adv. Energy Mater.* 7 (2017), 1700020.
- [31] Z. Li, J. Liang, Q. Liu, L. Xie, L. Zhang, Y. Ren, L. Yue, N. Li, B. Tang, A. Alshehri, M. Hamdy, Y. Luo, Q. Kong, X. Sun, High-efficiency ammonia electrosynthesis via selective reduction of nitrate on $ZnCo_2O_4$ nanosheet array, *Mater. Today Phys.* 23 (2022), 100619.
- [32] T. Wu, H. Zhao, X. Zhu, Z. Xing, Q. Liu, T. Liu, S. Gao, S. Lu, G. Chen, A. Asiri, Y. Zhang, X. Sun, Identifying the origin of Ti^{3+} activity toward enhanced electrocatalytic N_2 reduction over TiO_2 nanoparticles modulated by mixed-valent copper, *Adv. Mater.* 32 (2020), 2000299.
- [33] T. Wu, X. Zhu, Z. Xing, S. Mou, C. Li, Y. Qiao, Q. Liu, Y. Luo, X. Shi, Y. Zhang, X. Sun, Greatly improving electrochemical N_2 reduction over TiO_2 nanoparticles by iron doping, *Angew. Chem. Int. Ed.* 58 (2019) 18449–18453.
- [34] D. Jang, J. Maeng, J. Kim, H. Han, G. Park, J. Ha, D. Shin, Y. Hwang, W. Kim, Boosting electrocatalytic nitrate reduction reaction for ammonia synthesis by plasma-induced oxygen vacancies over $MnCoO_x$, *Appl. Surf. Sci.* 610 (2023), 155521.
- [35] Y. Chen, J. He, H. Pang, P. Jiang, F. Qu, D. Yu, J. Zhang, New insight into electrochemical denitrification using a self-organized nanoporous $VO-Co_3O_4/Co$ cathode: plasma-assistant oxygen vacancies catalyzed efficient nitrate reduction, *Sci. Total Environ.* 850 (2022), 157845.
- [36] X. Zhang, C. Wang, Y. Guo, B. Zhang, Y. Wang, Y. Yu, Cu clusters/ TiO_{2-x} with abundant oxygen vacancies for enhanced electrocatalytic nitrate reduction to ammonia, *J. Mater. Chem. A* 10 (2022) 6448–6453.
- [37] T. Feng, F. Li, X. Hu, Y. Wang, Selective electroreduction of nitrate to ammonia via $NbWO_6$ perovskite nanosheets with oxygen vacancy, *Chin. Chem. Lett.* (2022), 107862.
- [38] A. Kumar, T. Dixit, I. Palani, P. Sagdeo, V. Singh, Phase transformation and optical properties of annealed hydrothermally synthesized $ZnO/ZnCr_2O_4$ nanocomposites, *Int. J. Appl. Ceram. Tec.* 13 (2016) 912–919.
- [39] M. McCoy, R. Grimes, W. Lee, Planar intergrowth structures in the $ZnO-In_2O_3$ system, *Philos. Mag.* A 76 (1997) 1187–1201.
- [40] H. Song, D. Laudenschlager, J. Carey, H. Ruland, M. Nolan, M. Muhler, Spinel-structured $ZnCr_2O_4$ with excess Zn is the active ZnO/Cr_2O_3 catalyst for high-temperature methanol synthesis, *ACS Catal.* 7 (2017) 7610–7622.
- [41] W. Huang, W. Zha, D. Zhao, S. Feng, The effect of active oxygen species in nano- $ZnCr_2O_4$ spinel oxides for methane catalytic combustion, *Solid State Sci.* 87 (2019) 49–52.
- [42] X. Tian, C. Guo, H. Zhong, Y. Zhou, J. Xiao, Exceptional stability and chemical mechanism over spinel $ZnCr_2O_4$ catalyst for HCl oxidation to Cl_2 , *Mol. Catal.* 470 (2019) 82–88.
- [43] Y. Wang, A. Jia, M. Luo, J. Lu, Highly active spinel type $CoCr_2O_4$ catalysts for dichloromethane oxidation, *Appl. Catal. B Environ.* 165 (2015) 477–486.
- [44] Y. Gao, L. Zhang, A. Hoof, H. Friedrich, E. Hensen, A. Robust, $Au/ZnCr_2O_4$ catalyst with highly dispersed gold nanoparticles for gas-phase selective oxidation of cyclohexanol to cyclohexanone, *ACS Catal.* 9 (2019) 11104–11115.
- [45] A. Ismail, S. Albukhari, M. Mahmoud, Mesoporous $ZnCr_2O_4$ photocatalyst with highly distributed PtO nanoparticles for visible-light-induced photoreduction of nitrobenzene, *Opt. Mater.* 122 (2021), 111676.
- [46] L. Wang, X. Gao, Y. Bai, M. Tan, K. Sun, T. Zhang, Y. Wu, J. Pan, H. Xie, Y. Tan, The synergistic effect between ZnO and $ZnCr_2O_4$ on the catalytic performance for isobutanol synthesis from syngas, *Fuel* 253 (2019) 1570–1577.
- [47] G. Palanisamy, T. Pazhanivel, K. Bhuvanawari, G. Bharathi, G. Marimuthu, T. Maiyalagan, Spinel oxide $ZnCr_2O_4$ incorporated with ZnS quantum dots for application on visible light driven photocatalyst Azo dye degradation, *Colloids Surf. A* 590 (2020), 124505.
- [48] Z. Mekhalif, L. Massi, F. Guittard, S. Geribaldi, J. Delhalle, X-Ray photoelectron spectroscopy study of polycrystalline zinc modified by n-dodecanethiol and 3-perfluorooctyl-propanethiol, *Thin Solid Films* 405 (2002) 186–193.
- [49] R. Guttur, Sreekanth T. V. M., R. Rajavaram, D. PBorelli, D. Borelli, Nagajyothi P. C., J. Shim, Effect of reaction time and PVP contents on morphologies of hierarchical 3D flower-like $ZnCo_2O_4$ microstructures for energy storage devices, *Int. J. Energy Res.* 44 (2020) 11233–11247.
- [50] J. Gao, B. Jiang, C. Ni, Y. Qi, Y. Zhang, N. Oturan, M. Oturan, Non-precious $Co_3O_4-TiO_2$ /Ti cathode based electrocatalytic nitrate reduction: preparation, performance and mechanism, *Appl. Catal. B Environ.* 254 (2019) 391–402.
- [51] J. Hong, Y. Du, H. Zhang, W. Xue, K. San Hui, G. Fang, Electrochemical nitrate removal by magnetically immobilized nZVI anode on ammonia-oxidizing plate of RuO_2-Fe_3C , *Chemosphere* 294 (2022), 133806.
- [52] Y. Wang, L. Zhang, Y. Niu, D. Fang, J. Wang, Q. Su, C. Wang, Boosting NH_3 production from nitrate electroreduction via electronic structure engineering of Fe_3C nanoflakes, *Green Chem.* 23 (2021) 7594–7608.
- [53] S. Huo, S. Yang, Q. Niu, F. Yang, L. Song, Synthesis of functional Ni_2P/CC catalyst and the robust performances in hydrogen evolution reaction and nitrate reduction, *Int. J. Hydrog. Energy* 45 (2020) 4015–4025.
- [54] J. Wang, C. Cai, Y. Wang, X. Yang, D. Wu, Y. Zhu, M. Li, M. Gu, M. Shao, Electrocatalytic reduction of nitrate to ammonia on low-cost ultrathin CoO_x nanosheets, *ACS Catal.* 11 (2021) 15135–15140.
- [55] Z. Zhang, T. Fujioka, T. Koide, Y. Yano, T. Ono, Y. Hisaeda, Synthesis of first antimony porphyrane and electrocatalytic hydrogen evolution driven by ligand-centered reduction, *B. Chem. Soc. JPN* 94 (2021) 2048–2053.
- [56] Q. Li, Y. Liu, Z. Wan, H. Cao, S. Zhang, Y. Zhou, X. Ye, X. Liu, D. Zhang, Microwave-assisted synthesis of oxygen vacancy associated TiO_2 for efficient photocatalytic nitrate reduction, *Chin. Chem. Lett.* 33 (2022) 3835–3841.
- [57] M. Ehrenburg, A. Danilov, I. Botryakova, E. Molodkina, A. Rudnev, Electroreduction of nitrate anions on cubic and polyoriented platinum nanoparticles modified by copper adatoms, *J. Electroanal. Chem.* 802 (2017) 109–117.
- [58] S. Franz, H. Arab, G. Chiarello, M. Bestetti, E. Selli, Single-step preparation of large area TiO_2 photoelectrodes for water splitting, *Adv. Energy Mater.* 10 (2020), 2000652.
- [59] Y. Guo, R. Zhang, S. Zhang, Y. Zhao, Q. Yang, Z. Huang, B. Dong, C. Zhi, Pd doping-weakened intermediate adsorption to promote electrocatalytic nitrate reduction on TiO_2 nanoarrays for ammonia production and energy supply with zinc-nitrate batteries, *Energy Environ. Sci.* 14 (2021) 3938–3944.
- [60] G. Henkelman, A. Arnaldsson, H. Jónsson, A fast and robust algorithm for Bader decomposition of charge density, *Comput. Mater. Sci.* 36 (2006) 354–360.
- [61] B. Hammer, J. Nørskov, Theoretical surface science and catalysis—calculations and concepts, in: *Advances in Catalysis* vol. 45, Academic Press, 2000, pp. 71–129.
- [62] V. Deringer, A. Tchougréeff, R. Dronskowski, Crystal orbital hamilton population (COHP) analysis as projected from plane-wave basis sets, *J. Phys. Chem. A* 115 (2011) 5461–5466.